

Article

Exploring the Crystalline Structure of Gold Mesocrystals Using X-ray Diffraction

Aleksandra Chumakova ^{1,2,*}, Felizitas Kirner ³ , Andrei Chumakov ⁴ , Stephan V. Roth ^{4,5}, Alexei Bosak ^{2,*} and Elena V. Sturm ^{3,*}

¹ Outstation at Heinz Maier-Leibnitz Zentrum (MLZ), Institute of Crystallography (IfK), RWTH Aachen University, Lichtenbergstrasse 1, 85747 Garching, Germany

² European Synchrotron Radiation Facility, 71 Avenue des Martyrs, 38000 Grenoble, France

³ Department of Earth and Environmental Sciences, Section of Crystallography, Ludwig-Maximilians-Universität München (LMU), Theresienstr. 41C, 80333 Munich, Germany

⁴ Deutsches Elektronen-Synchrotron DESY, Notkestr. 85, 22607 Hamburg, Germany; svroth@kth.se (S.V.R.)

⁵ Department of Fibre and Polymer Technology, KTH Royal Institute of Technology, Teknikringen 56-58, 10044 Stockholm, Sweden

* Correspondence: chumakova@ifk.rwth-aachen.de (A.C.); alexei.bosak@esrf.fr (A.B.); sturm.elena@lmu.de (E.V.S.)

Abstract: Mesocrystals are a class of nanostructured material where individual nanocrystals are arranged in a distinct crystallographic orientation. The multiple-length-scale order in such materials plays an essential role in the emergent physical and chemical phenomena. Our work studies the structure of a faceted mesocrystal composed of polystyrene-functionalized single crystalline gold nanoparticles using complementary ultrasmall- and wide-angle X-ray scattering (USAXS and WAXS) with electron microscopy. The results of the data analysis shed some light on the details of the microscopic structure of mesocrystals and their structuration principle.

Keywords: mesocrystal; gold nanoparticles; small-angle X-ray diffraction; wide-angle X-ray diffraction; supercrystallography



Citation: Chumakova, A.; Kirner, F.; Chumakov, A.; Roth, S.V.; Bosak, A.; Sturm, E.V. Exploring the Crystalline Structure of Gold Mesocrystals Using X-ray Diffraction. *Crystals* **2023**, *13*, 1204. <https://doi.org/10.3390/cryst13081204>

Academic Editor: Carlos Rodriguez-Navarro

Received: 19 June 2023

Revised: 19 July 2023

Accepted: 24 July 2023

Published: 2 August 2023



Copyright: © 2023 by the authors. Licensee MDPI, Basel, Switzerland. This article is an open access article distributed under the terms and conditions of the Creative Commons Attribution (CC BY) license (<https://creativecommons.org/licenses/by/4.0/>).

1. Introduction

Mesocrystals are solids that form when nanoscale crystals assemble into a pattern with long-range order on the atomic scale. Compared with conventional crystals, the mesocrystal structure's short- (atomic) and long-range (interparticle) periodicities allow for the emergence of unique physical and chemical properties [1]. Therefore, these materials have been studied for their potential use in various applications [2–4], including catalytic [5,6], optical, electronic [7], and pharmaceutical fields, i.e., biosensors and drug delivery [8,9].

In recent years, the synthesis of nanoparticles has become more advanced, granting access to nanoparticles with well-defined sizes and shapes. The optimization of the assembly conditions of these nanoparticles has generated mesocrystals with impressive structural diversity [10–12]. However, analysis of the influence of structural defects or modulations in the properties of experimentally created self-assembled objects has been rare and mostly limited to studies on close-packed arrays of spheres. For instance, studies on colloidal crystals of micrometer-sized spheres have shown that defects such as vacancies, dislocations, and grain boundaries can generate nonlinear stress fields that affect the mechanical properties of the assemblies [5].

Carnis et al. used coherent X-ray diffraction imaging to explore the 3D structure and defects of a small self-assembled gold mesocrystal grain built from single crystalline cubic nanoparticles. In addition, the reconstructed electron density of the gold mesocrystal revealed its intrinsic structural heterogeneity, including local deviations of lattice parameters and internal defects. The strain distribution showed that the average superlattice and the

real “multidomain” structure of the mesocrystal were very close [13]. Mayence et al. used 3D small-angle electron diffraction tomography to show stacking faults in spherical Pd nanoparticle superlattices and built some analogies to the dislocations in close-packed metals. Time-resolved SAXS and grazing-incidence SAXS (GISAXS) have been mainly used to gain an insight into the structural evolution of mesocrystals [14].

The standard methods to characterize mesocrystals are electron microscopy and X-ray-scattering/diffraction-based techniques; these techniques offer a unique set of advantages and disadvantages [12,15]. In particular, scanning or transmission electron microscopy (SEM or TEM) allow the obtention of detailed information on the structure in real space but only at the surface or limited to the sub-surface volume. An extended internal structure of the test sample can only be revealed upon the stepwise investigation of the sample layers and sequential removal/destruction of the top layers. This may be achieved by a combination of electron microscopy and the FIB technique. The possible drawbacks are induced artifacts by softening and the movement of the particles in their superstructure at the conditions necessary for FIB cutting [13]. In contrast, X-ray scattering easily provides quantitative information from the entire irradiated sample volume; however, this is encoded in the reciprocal space. Periodic structures can be probed on multiple length scales, routinely down to an atomic-scale resolution as in conventional X-ray crystallography. SAXS examines the length scale of nanoparticles in their superstructures and can be augmented with wide-angle X-ray scattering (WAXS) when the atomic scale and relative orientations of the particles become the subject of interest. In contrast to the previously employed approach with coherent X-ray diffraction imaging, the investigated sample can be significantly larger, avoiding artifacts through preprocessing procedures.

The main scope of this study is to further benchmark and advance a methodological approach for the non-destructive characterization of highly ordered nanostructured materials across multiple structural levels. We combined electron microscopy (SEM and TEM) with diffraction techniques, namely SAXS/WAXS and ultra SAXS (USAXS), to improve our understanding of the internal structure of the self-assembled gold mesocrystals.

2. Materials and Methods

2.1. Chemicals and Materials

Milli-Q water (resistivity 18.2 M Ω cm) was used in all experiments. If not otherwise stated, all chemicals were bought and used as received. Hydrogen tetrachloroaurate trihydrate (HAuCl₄ · 3H₂O, $\geq 99.9\%$), hexadecyltrimethylammonium bromide (CTAB, $\geq 99\%$), cetyltrimethylammonium chloride solution (CTAC, 25 wt% in H₂O), and hexadecylpyridinium chloride monohydrate (CPC, 99.0–102.0%) were purchased from Sigma-Aldrich[®], Darmstadt, Germany. Sodium borohydride (NaBH₄, $\geq 97\%$) and L(+)-ascorbic acid (AA, $\geq 99\%$) were purchased from Carl Roth. Potassium bromide (KBr, for IR spectroscopy) was purchased from Merck KGaA. ω -Thiol-terminated polystyrene (M_N = 43 kg/mol) was purchased from Polymer Source Inc. THF ($\geq 99.5\%$, stabilized) and toluene ($\geq 99.5\%$) were purchased from VWR.

2.2. Synthesis of Gold Nanoparticles

2.2.1. Synthesis of Initial Seeds

An aqueous solution of HAuCl₄ (0.25 mL, 0.01 M) and CTAB (7.50 mL, 0.10 M) was mixed in a glass vial (50 mL) and tempered to 27 °C. A total of 0.60 mL of 0.01 M freshly prepared ice-cold NaBH₄ was added under vigorous stirring. The resulting solution turned brown immediately. The seed solution was aged for 90 min at 27 °C to ensure the complete decomposition of excess borohydride.

2.2.2. Synthesis of Spherical Seeds

The synthesis of spherical seeds was adapted from Zheng et al. [16]. Aqueous solutions of CTAC (39.00 mL, 0.10 M) and HAuCl₄ (1.00 mL, 0.01 M) were mixed in a glass vial (100 mL) and tempered to 27 °C. AA (15.00 mL, 0.10 M) was added, followed by a rapid

injection of 500 μL of the initial seeds. The solution turned red immediately and was kept at 27 $^{\circ}\text{C}$ for 15 min. The spherical seeds were collected by centrifugation at 30,000 rpm for 120 min and were washed once with water and twice with 0.02 M CPC solution. The optical density of the dispersion was adjusted to 0.275 (approx. 1×10^{12} particles/mL).

2.2.3. Synthesis of Cubic Nanoparticles

The synthesis of the cubic nanoparticles was adapted from previous work [17]. Aqueous solutions of HAuCl_4 (1.00 mL, 0.01 M), KBr (125 μL , 0.04 M), and CPC (50.00 mL, 0.10 M) were mixed in a glass vial (100 mL) and tempered to 27 $^{\circ}\text{C}$. An aqueous solution of AA (1.50 mL, 0.01 M) was added, followed by a rapid injection of 800 μL of the washed spherical seeds. The solution turned pinkish red and was kept at 27 $^{\circ}\text{C}$ for 3 h. The NPs were collected by centrifugation at 9000 rpm for 5 min and redispersed in 0.02 M CPC solution. The particles were characterized using UV/Vis and TEM (Figure 1a–d). TEM characterization revealed an edge length of 47.6 nm.

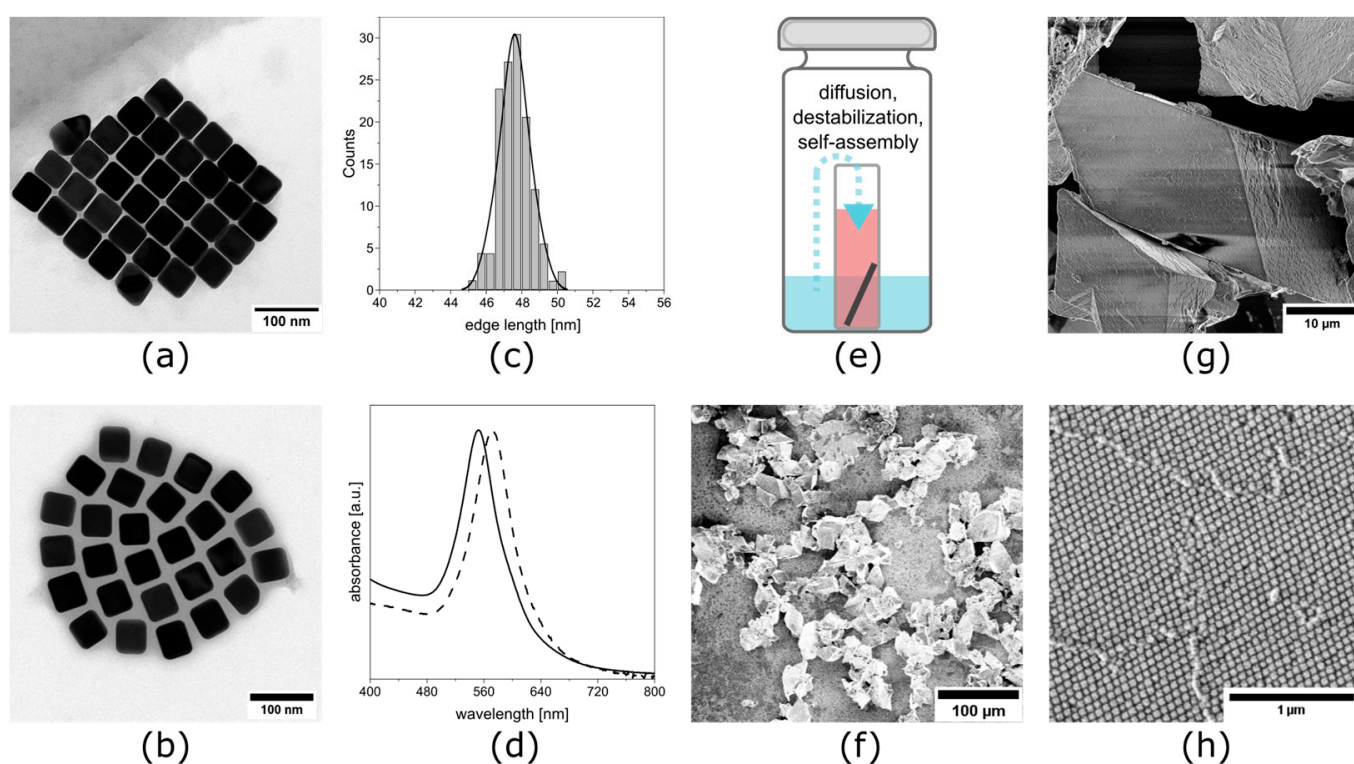


Figure 1. The gold nanocubes were synthesized and characterized and then assembled into mesocrystals. (a) TEM image of cubic gold nanoparticles as synthesized by aqueous dispersion. (b) TEM after functionalization with ω -thiol-terminated polystyrene and the related phase transfer. (c) The median edge length of 47.6 ± 0.9 nm was determined from TEM images using Fiji [18]. (d) UV/Vis spectroscopy showed a single peak for both nanoparticle dispersions (solid–aqueous and dotted–toluene), proving no larger aggregates were already present in the solution. (e) Sketch of an experimental gas-phase diffusion setup for the mesocrystal self-assembly. (f,g) SEM images of the as synthesized mesocrystals with (h) a close-up view of the individual nanoparticles.

2.2.4. Functionalization of Cubic Nanoparticles with PS-SH and Dispersion in Toluene

The functionalization of the gold nanoparticles was adapted from a procedure described by Sánchez-Iglesias et al. [19]. The dispersed nanoparticles were concentrated to 1 mg/mL. An amount of 1 mL of this dispersion was added to 10 mL THF containing 0.46 mg of ω -thiol-terminated polystyrene before mixing thoroughly. The dispersion was left undisturbed for 12 h and then centrifuged at 9000 rpm for 5 min. The supernatant was discarded and the tube refilled to 10 mL with THF. Again, the dispersion was centrifuged

at 9000 rpm for 5 min and the supernatant was carefully discarded. The sediment was then redispersed in 500 μL of toluene to a final concentration of 2 mg/mL. The particles were characterized using UV/Vis and TEM (Figure 1a–d).

2.3. Self-Assembly to Mesocrystals

The nanocubes were assembled into mesocrystals using a gas-phase diffusion technique (Figure 1e). An amount of 400 μL of the 2 mg/mL nanocube dispersion in toluene was added to a 1 mL flat-bottom vial containing a silicon snippet. This small vial was then placed in a larger vial containing an antisolvent that consisted of 1.5 mL ethanol and 1.5 mL toluene. The larger vial was sealed, creating a closed system. The antisolvent diffused over the gas phase into the nanoparticle dispersion, destabilizing the particles. Consequently, the particles self-assembled, which was indicated by a gradual discoloration of the dispersion. After 4 weeks, the solution was fully clear and was carefully removed using a syringe. The silicon snippet was subsequently dried using a careful flow of air, leaving the faceted mesocrystals (Figure 1f–h).

2.4. Diffraction Data Collection

An individual mesocrystal with a size of about $60 \times 60 \times 60 \mu\text{m}^3$ was fixed on a glass fiber for diffraction experiments.

WAXS/SAXS: The ambient temperature diffraction data were collected at the diffractometer on the ID28 beamline at the ESRF (Grenoble, France) at the wavelengths $\lambda = 0.697 \text{ \AA}$ and $\lambda = 0.980 \text{ \AA}$; the typical beam size was about 40 μm full width at half maximum (FWHM) [20]. A single-photon counting PILATUS3 1M detector with a pixel size $172 \times 172 \mu\text{m}^2$ was used for data recording; it was positioned at sample–detector distances (SDDs) of 244 mm or 414 mm and used in shutterless mode over a sample rotation of 360° with 0.25° steps. The pixel size of the detector essentially dominates the experimental momentum resolution for the given data under such experimental parameters as the sample size, beam size, and divergence.

USAXS: The ultrasmall-angle diffraction measurements were performed at the P03 beamline at the synchrotron PETRA III at DESY (Hamburg, Germany) [21,22]. The USAXS measurements were performed in transmission geometry with an X-ray wavelength $\lambda = 1.048 \text{ \AA}$ ($E = 11.83 \text{ keV}$), an SDD of 9505 mm, and over a rotation of 360° with 1° steps around the vertical rotation axis. The beam size was $73 \times 71 \mu\text{m}^2$ (Horiz. \times Vert.), and a single-photon counting detector (PILATUS 2M, Dectris) with a pixel size of $172 \times 172 \mu\text{m}^2$ was used to record the scattering patterns.

In both cases, the experimental geometry and the orientation matrix were refined using CrysAlisPro software [23] and the best-matched superlattice symmetry was then determined. The locally developed software was used for high-resolution 2D reconstructions and for the selected area and selected volume intensity integration. By combining synchrotron-based X-ray scattering/diffraction techniques, we were able to reconstruct the mesocrystal structure from the atomic to the mesoscopic scales. A combined linear–logarithmic scale was employed for 2D scattering data visualization, as this is conveniently implemented in the Albula software [24]

3. Results and Discussion

Mesocrystals were assembled from polystyrene-functionalized gold nanocubes with 48 nm edge lengths. A single mesocrystal was picked for the further analysis as described in the Methods section. A scanning electron micrograph of an exemplary gold mesocrystal is shown in the Figure 2.

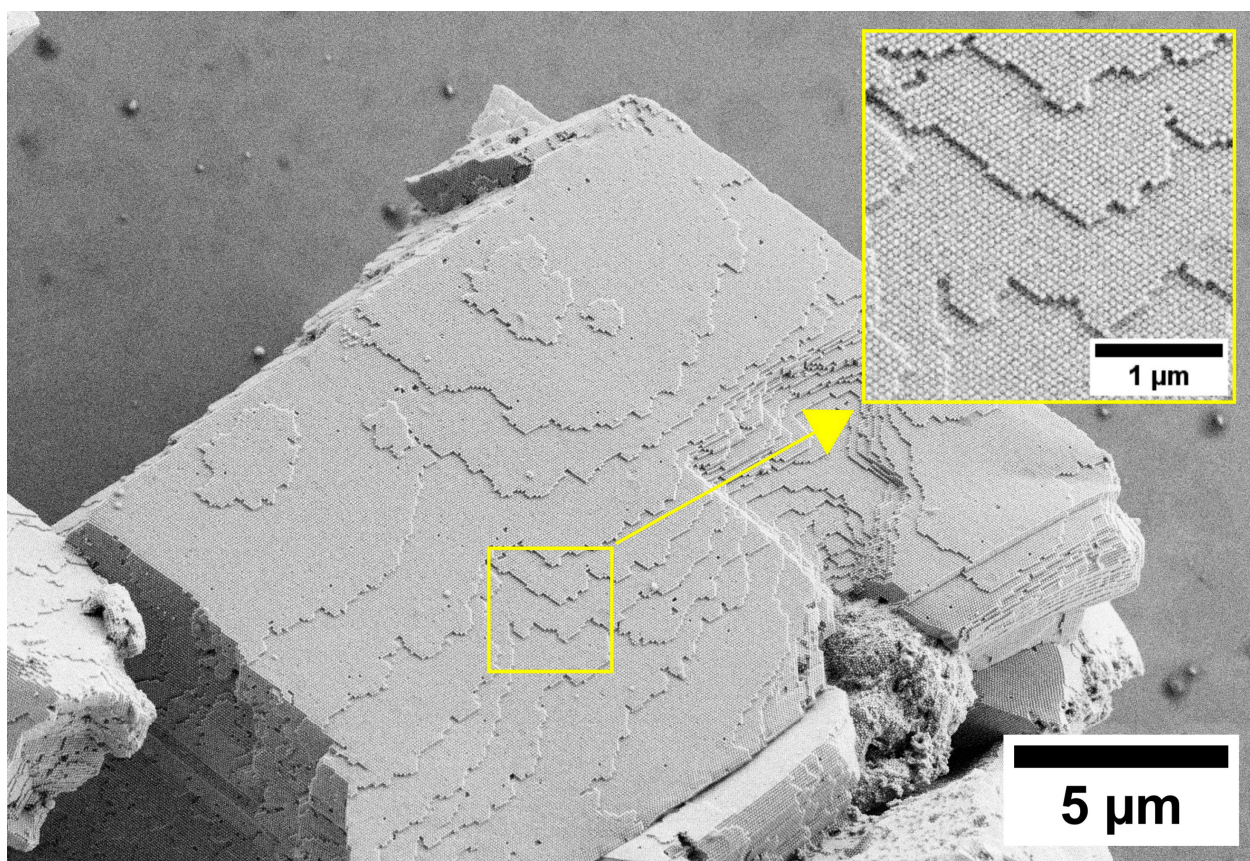


Figure 2. SEM image of an exemplary mesocrystal built from cubic gold nanocrystals interspaced by ω -thiol-terminated polystyrene. The packing pattern of the individual nanoparticles on the mesocrystal surface is clearly resolvable (inset figure).

The typical wide-field reconstructions of high-symmetry gold planes $h0l$ and hhl are shown in Figure 3a,b. There are pronounced diffuse lines emerging from Bragg reflections and the 000 node, propagating along $\langle 100 \rangle$ -type directions; the lines from 200 to 000 are the most pronounced and the square grid of intersecting lines is nicely visible in the $h0l$ plane. In the combined SAXS/WAXS measurement, the small-angle part essentially remains unresolved, so we complemented our study with USAXS (Figure 3c,d). The precise orientational relationships between the atomic structures of individual cubic nanoparticles and the self-ordered assembly were established by combining the datasets.

High-symmetry USAXS reconstructions of the $h0l$ and hhl planes in the mesocrystal's rhombohedral basis are shown in Appendix A Figure A1. The USAXS studies show the outstanding packing perfection of the mesocrystals: more than 10 diffraction orders are visible without any remarkable angular spread.

Gold nanocrystals are packed to the rhombohedral superlattice ($R\bar{3}m$). The unit cell parameters are refined as $a_{SL} = 62.9 \pm 0.12$ nm and $\alpha_{SL} = 69.5^\circ \pm 0.2^\circ$. It is important to emphasize that the rhombohedral structure is firmly linked to the cubic lattice $\langle 111 \rangle_{Au} \parallel \langle 111 \rangle_{SL}, \langle 1\bar{1}0 \rangle_{Au} \parallel \langle 1\bar{1}0 \rangle_{SL}$. This value is significantly larger than only the edge length of the nanocubes, accounting for the polystyrene on the particle surface. This polymer is observable in the TEM image Figure 1b as a grey “shadow” interspacing the gold nanocubes.

The WAXS measurements confirm that the gold nanoparticles possess the expected face-centered cubic (fcc) structure with a lattice parameter of $a = 4.087 \pm 0.005$ Å [25]. The radial and azimuthal broadening around the 200 node were analyzed in detail. The azimuthal broadening shape is due to the orientation distribution function, with the distribution of tilts being close to isotropic. The angular spread in the main orthogonal directions

is about 3.9° and 4.6° and anisotropy is compatible with rhombohedral packing symmetry (Appendix A Figure A2). Close inspection reveals interference ripples in the radial direction (Figure 4), meaning the WAXS pattern represents the incoherent sum of the coherent scattering events of the individual nanoparticles. The observation of ripples over many orders of magnitude points to the narrow dispersion of facet-to-facet intraparticle distance along $\langle 100 \rangle$. As a first approximation, the position of the minima/maxima, as well as decay of oscillation, can be treated within a simple model where the intensity is approximated using Equation (1)

$$I \sim \text{sinc}^2(aD) \otimes \exp\left(\frac{-D^2}{2\sigma^2}\right),$$

(where a —lattice parameter of gold, D —distance between two parallel (hkl) facets, σ —spread) obtaining an estimate of the distance $D(100)$ between two parallel facets (100) of the nanoparticles as 51 nm and an estimate of its spread σ as 2 nm (Figure 4b). A proper error estimate is not possible since an appropriate fitting procedure could not be applied. However, these values fit with the results obtained from TEM.

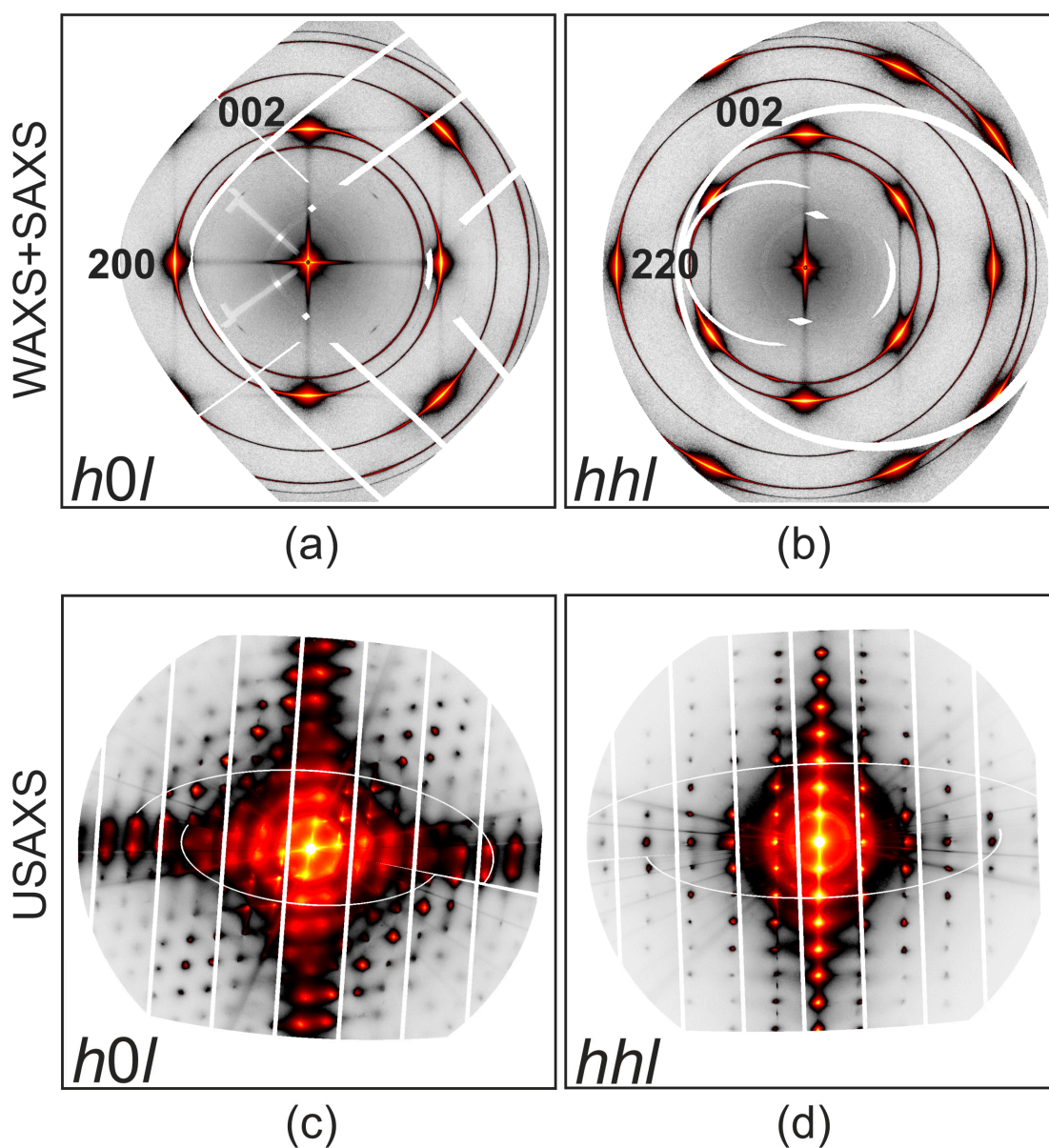


Figure 3. Reciprocal space reconstructions of $h0l$ and hhl planes of gold mesocrystals in cubic basis: (a,b) low-momentum-resolution WAXS/SAXS and (c,d) USAXS.

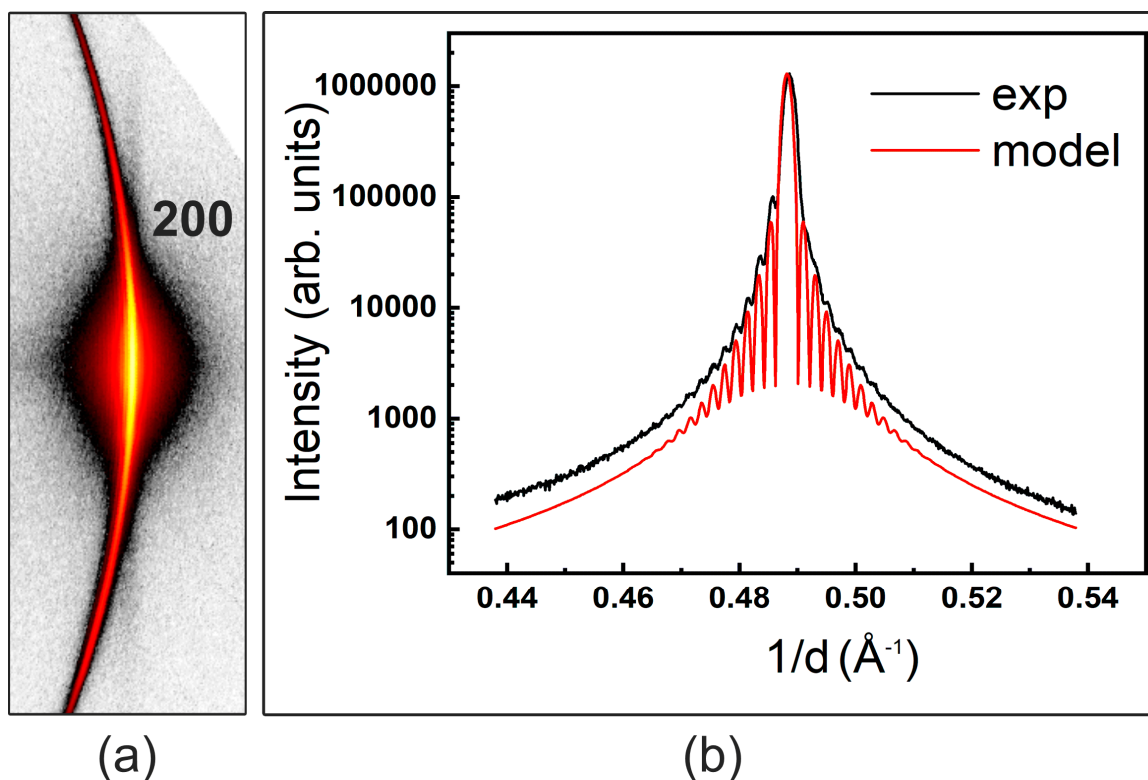


Figure 4. (a) High-symmetry reconstruction plane $h0l$ in the proximity of 200 gold spot. (b) The intensity profile in the radial direction across the 200 spot. The black line indicates the experimental data; the red line corresponds to the modeling.

No resolved ripples were observed along the 110 or 111 directions, indicating either a large facet-to-facet distance spread along those directions or their small surface. Some insights could be obtained from the considerations of a packing mode with a fixed surface shell thickness [26]. Comparing the packing periodicity with $D(100)$, we calculate the shell thickness as ~ 5 nm and $D(110)$ as ~ 62 nm. We could not constrain $D(111)$ with the available information. The interparticle contact distance of 10 nm is in good agreement with the TEM data shown in Figure 1b. A corresponding model for the packing (with an exemplary but modest truncation of the nanocubes along $\langle 111 \rangle$ and $\langle 110 \rangle$) is shown in Figure 5.

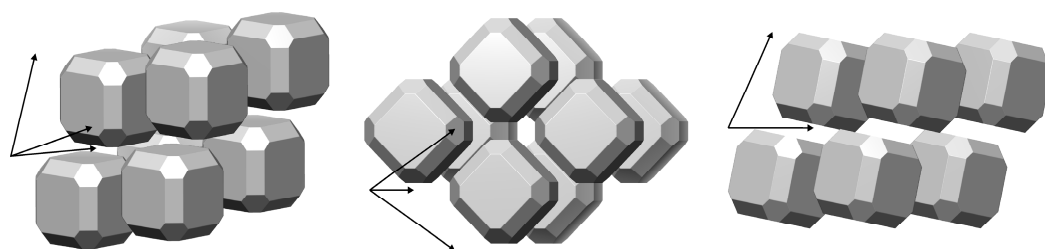


Figure 5. Packing of nanoparticles for rhombohedral structure. Truncation along $\langle 110 \rangle$ and $\langle 111 \rangle$ is introduced as described in text.

The above findings fit our previous observations on magnetite mesocrystals [25] that dominating (100) faces (i.e., a modest degree of truncation for the cubic particles) promote the formation of a rhombohedral superstructure. The observations for other systems show a similar trend [27–30]. Further work may enable the creation of a phase diagram relating the truncation type/degree to the packing mode.

4. Conclusions

We report the self-assembly of mesocrystals from polystyrene-functionalized gold nanoparticles with edge lengths of 48 nm. The mesocrystalline structure was studied in detail by combining electron microscopy techniques (SEM and TEM), SAXS/WAXS, and USAXS to cover an extended scale in real and reciprocal space in a consistent way. We find the gold nanocubes to be packed in a rhombohedral superlattice ($R\bar{3}m$) with $a_{\text{SL}} = 62.9 \pm 0.12$ nm and $\alpha_{\text{SL}} = 69.5^\circ \pm 0.2^\circ$. These results were obtained in a non-destructive manner and emphasize the potential of this combination of methods for the characterization of nanostructured materials across multiple structural levels. We conclude that, from the technical point of view, the collection of the diffraction data in the entire reciprocal space mapping was more beneficial than the selected zones approach typically used in standard SAXS studies [31].

Author Contributions: Conceptualization, A.C. (Aleksandra Chumakova), E.V.S. and A.B.; methodology, A.C. (Aleksandra Chumakova) and F.K.; software, A.B.; validation, A.C. (Aleksandra Chumakova), E.V.S., and A.B.; formal analysis, A.C. (Aleksandra Chumakova); investigation, A.C. (Aleksandra Chumakova); USAXS study, A.C. (Andrei Chumakov); resources, E.V.S., S.V.R., and A.B.; data curation, A.C. (Aleksandra Chumakova); writing—original draft preparation, A.C. (Aleksandra Chumakova) and F.K.; writing—review and editing, E.V.S. and A.C. (Andrei Chumakov); visualization, A.C. (Aleksandra Chumakova) and A.B.; supervision, E.V.S. and A.B. All authors have read and agreed to the published version of the manuscript.

Funding: This research was partially funded by DFG (Deutsche Forschungsgemeinschaft) SFB 1214, project B1.

Data Availability Statement: Not applicable.

Acknowledgments: We acknowledge DESY (Hamburg, Germany), a member of Helmholtz Association HGF, for the provision of experimental facilities. Part of this research was carried out at PETRA III, and we would like to thank P03 beamline staff for their assistance.

Conflicts of Interest: The authors declare no conflict of interest.

Appendix A

Details of the Mesocrystal Synthesis

The gold nanocubes were synthesized according to the procedure described in the experimental section. TEM was used to verify the nanoparticle shape and ensure that the morphology was retained after functionalization with ω -thiol-terminated polystyrene and the related phase transfer (Figure 1a,b). The longer chain length of the polymer compared with the C14 chain of the CPC manifests in a larger interparticle distance within the dried sample. The median edge length was determined from TEM images using Fiji [18]. The edge length corresponds to the minimum Feret's diameter and was 47.6 ± 0.9 nm (Figure 1c). UV/Vis spectroscopy showed a single peak for both nanoparticle dispersions (solid—aqueous; dotted—toluene), proving no larger aggregates were present in the solution before initializing the self-assembly. The red shift after functionalization was due to changes in the environmental conditions of the nanocubes. Figure 1e depicts a sketch of an experimental setup for the mesocrystal self-assembly. The antisolvent ethanol (blue) diffuses over the gas phase (dotted arrow) into the nanoparticle dispersion (red). Ethanol is a bad solvent for the polystyrene and leads to the collapse of the polymer and destabilization of the nanoparticle dispersion. The particles self-assemble into larger structures that sediment onto the silicon snippet (dark grey).

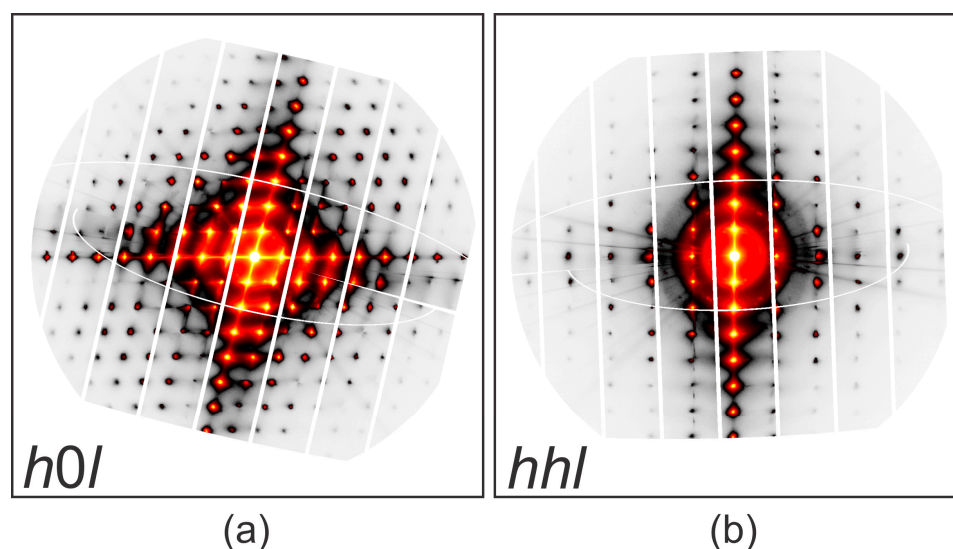


Figure A1. Reciprocal space reconstructions of the $h0l$ (a) and hhl (b) planes of gold mesocrystals in rhombohedral basis: USAXS data.

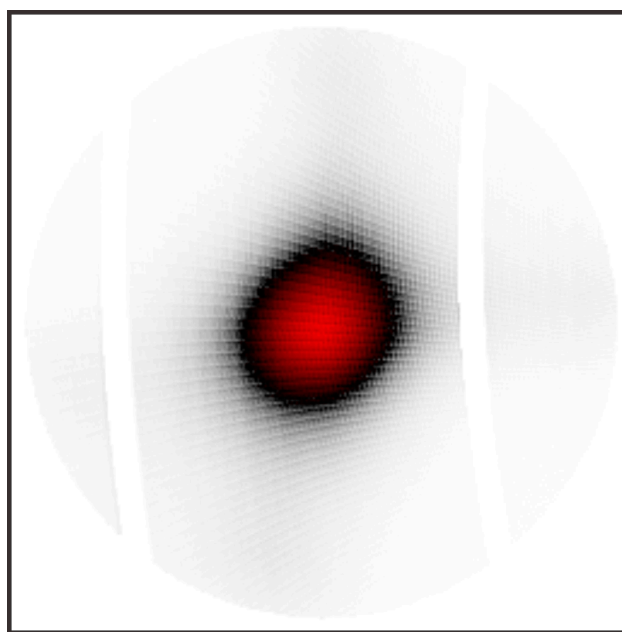


Figure A2. Azimuthal intensity distribution for the 200 gold spot within a $\sim 10 \times 10 \text{ deg}^2$ range.

References

1. Fang, J.; Ding, B.; Gleiter, H. Mesocrystals: Syntheses in Metals and Applications. *Chem. Soc. Rev.* **2011**, *40*, 5347–5360. [[CrossRef](#)]
2. Zhou, L.; O'Brien, P. Mesocrystals—Properties and Applications. *J. Phys. Chem. Lett.* **2012**, *3*, 620–628. [[CrossRef](#)]
3. Ma, M.G.; Cölfen, H. Mesocrystals—Applications and Potential. *Curr. Opin. Colloid Interface Sci.* **2014**, *19*, 56–65. [[CrossRef](#)]
4. Ni, B.; Gonzalez-Rubio, G.; Cölfen, H. Self-Assembly of Colloidal Nanocrystals into 3D Binary Mesocrystals. *Acc. Chem. Res.* **2022**, *55*, 1599–1608. [[CrossRef](#)] [[PubMed](#)]
5. Zhang, P.; Ochi, T.; Fujitsuka, M.; Kobori, Y.; Majima, T.; Tachikawa, T.; Zhang, D.; Fujitsuka, M.; Majima, T.; Ochi, T.; et al. Topotactic Epitaxy of SrTiO₃ Mesocrystal Superstructures with Anisotropic Construction for Efficient Overall Water Splitting. *Angew. Chem. Int. Ed.* **2017**, *56*, 5299–5303. [[CrossRef](#)]
6. Sun, S.; Yu, X.; Yang, Q.; Yang, Z.; Liang, S. Mesocrystals for Photocatalysis: A Comprehensive Review on Synthesis Engineering and Functional Modifications. *Nanoscale Adv.* **2019**, *1*, 34–63. [[CrossRef](#)] [[PubMed](#)]
7. Yamada, K.; Kohiki, S. Dielectric and Optical Properties of BaTiO₃ Mesocrystals. *Phys. E Low-Dimens. Syst. Nanostruct.* **1999**, *4*, 228–230. [[CrossRef](#)]
8. Lee, T.; Zhang, C.W. Dissolution Enhancement by Bio-Inspired Mesocrystals: The Study of Racemic (R,S)-(\pm)-Sodium Ibuprofen Dihydrate. *Pharm. Res.* **2008**, *25*, 1563–1571. [[CrossRef](#)] [[PubMed](#)]

9. Uchaker, E.; Cao, G. Mesocrystals as Electrode Materials for Lithium-Ion Batteries. *Nano Today* **2014**, *9*, 499–524. [CrossRef]
10. Wetterskog, E.; Agthe, M.; Mayence, A.; Grins, J.; Wang, D.; Rana, S.; Ahniyaz, A.; Salazar-Alvarez, G.; Bergström, L. Precise Control over Shape and Size of Iron Oxide Nanocrystals Suitable for Assembly into Ordered Particle Arrays. *Sci. Technol. Adv. Mater.* **2014**, *15*, 055010. [CrossRef]
11. Disch, S.; Wetterskog, E.; Hermann, R.P.; Salazar-Alvarez, G.; Busch, P.; Brückel, T.; Bergström, L.; Kamali, S. Shape Induced Symmetry in Self-Assembled Mesocrystals of Iron Oxide Nanocubes. *Nano Lett.* **2011**, *11*, 1651–1656. [CrossRef]
12. Li, R.; Zhang, J.; Tan, R.; Gerdes, F.; Luo, Z.; Xu, H.; Hollingsworth, J.A.; Klinke, C.; Chen, O.; Wang, Z. Competing Interactions between Various Entropic Forces toward Assembly of Pt₃Ni Octahedra into a Body-Centered Cubic Superlattice. *Nano Lett.* **2016**, *16*, 2792–2799. [CrossRef]
13. Carnis, J.; Kirner, F.; Lapkin, D.; Sturm, S.; Kim, Y.Y.; Baburin, I.A.; Khubbutdinov, R.; Ignatenko, A.; Iashina, E.; Mistonov, A.; et al. Exploring the 3D Structure and Defects of a Self-Assembled Gold Mesocrystal by Coherent X-Ray Diffraction Imaging. *Nanoscale* **2021**, *13*, 10425–10435. [CrossRef] [PubMed]
14. Mayence, A.; Wang, D.; Salazar-Alvarez, G.; Oleynikov, P.; Bergström, L. Probing Planar Defects in Nanoparticle Superlattices by 3D Small-Angle Electron Diffraction Tomography and Real Space Imaging. *Nanoscale* **2014**, *6*, 13803–13808. [CrossRef]
15. Mourdikoudis, S.; Pallares, R.M.; Thanh, N.T.K. Characterization Techniques for Nanoparticles: Comparison and Complementarity upon Studying Nanoparticle Properties. *Nanoscale* **2018**, *10*, 12871–12934. [CrossRef] [PubMed]
16. Zheng, Y.; Ma, Y.; Zeng, J.; Zhong, X.; Jin, M.; Li, Z.Y.; Xia, Y. Seed-Mediated Synthesis of Single-Crystal Gold Nanospheres with Controlled Diameters in the Range 5–30 Nm and Their Self-Assembly upon Dilution. *Chem. Asian J.* **2013**, *8*, 792–799. [CrossRef]
17. Kirner, F.; Potapov, P.; Schultz, J.; Geppert, J.; Müller, M.; González-Rubio, G.; Sturm, S.; Lubk, A.; Sturm, E. Additive-Controlled Synthesis of Monodisperse Single Crystalline Gold Nanoparticles: Interplay of Shape and Surface Plasmon Resonance. *J. Mater. Chem. C* **2020**, *8*, 10844–10851. [CrossRef]
18. Schindelin, J.; Arganda-Carreras, I.; Frise, E.; Kaynig, V.; Longair, M.; Pietzsch, T.; Preibisch, S.; Rueden, C.; Saalfeld, S.; Schmid, B.; et al. Fiji: An Open-Source Platform for Biological-Image Analysis. *Nat. Methods* **2012**, *9*, 676–682. [CrossRef]
19. Sánchez-Iglesias, A.; Grzelczak, M.; Altantzis, T.; Goris, B.; Pérez-Juste, J.; Bals, S.; Van Tendeloo, G.; Donaldson, S.H.; Chmelka, B.F.; Israelachvili, J.N.; et al. Hydrophobic Interactions Modulate Self-Assembly of Nanoparticles. *ACS Nano* **2012**, *6*, 11059–11065. [CrossRef]
20. Girard, A.; Nguyen-Thanh, T.; Souliou, S.M.; Stekiel, M.; Morgenroth, W.; Paolasini, L.; Minelli, A.; Gambetti, D.; Winkler, B.; Bosak, A. A New Diffractometer for Diffuse Scattering Studies on the ID28 Beamline at the ESRF. *J. Synchrotron Radiat.* **2019**, *26*, 272–279. [CrossRef]
21. Krywka, C.; Neubauer, H.; Priebe, M.; Salditt, T.; Keckes, J.; Buffet, A.; Roth, S.V.; Doehrmann, R.; Mueller, M. A Two-Dimensional Waveguide Beam for X-ray Nanodiffraction. *J. Appl. Crystallogr.* **2011**, *45*, 85–92. [CrossRef]
22. Buffet, A.; Rothkirch, A.; Döhrmann, R.; Körstgens, V.; Abul Kashem, M.M.; Perlich, J.; Herzog, G.; Schwartzkopf, M.; Gehrke, R.; Müller-Buschbaum, P.; et al. P03, the Microfocus and Nanofocus X-ray Scattering (MiNaXS) Beamline of the PETRA III Storage Ring: The Microfocus Endstation. *J. Synchrotron Radiat.* **2012**, *19*, 647–653. [CrossRef] [PubMed]
23. CrysAlis Pro | Rigaku Global Website. Available online: <https://www.rigaku.com/products/crystallography/crysalis> (accessed on 22 March 2023).
24. DECTRIS ALBULA: Software for X-ray and Electron Detectors—Dectris. Available online: <https://www.dectris.com/detectors/albula-software/> (accessed on 21 March 2023).
25. Wyckoff, R.W.G. *Cubic Closest Packed, Ccp, Structure Crystal Structures*, 2nd ed.; Interscience Publishers: New York, NY, USA, 1963; Volume 1, pp. 7–83.
26. Chumakova, A.; Steegemans, T.; Baburin, I.A.; Mistonova, A.; Dubitskiy, I.S.; Schlottheuber, J.; Kirner, F.; Sturm, S.; Lubk, A.; Müller-Caspary, K.; et al. Multiscale Reciprocal Space Mapping of Magnetite Mesocrystals. *Adv. Mater.* **2023**, *35*, 2207130. [CrossRef] [PubMed]
27. Zhang, Y.; Lu, F.; Van Der Lelie, D.; Gang, O. Continuous Phase Transformation in Nanocube Assemblies. *Phys. Rev. Lett.* **2011**, *107*, 135701. [CrossRef] [PubMed]
28. Eggiman, B.W.; Tate, M.P.; Hillhouse, H.W. Rhombohedral Structure of Highly Ordered and Oriented Self-Assembled Nanoporous Silica Thin Films. *Chem. Mater.* **2006**, *18*, 723–730. [CrossRef]
29. Avci, C.; Imaz, I.; Carné-Sánchez, A.; Pariente, J.A.; Tasios, N.; Pérez-Carvajal, J.; Alonso, M.I.; Blanco, A.; Dijkstra, M.; López, C.; et al. Self-Assembly of Polyhedral Metal–Organic Framework Particles into Three-Dimensional Ordered Superstructures. *Nat. Chem.* **2017**, *10*, 78–84. [CrossRef]
30. Schulz, F.; Lokteva, I.; Parak, W.J.; Lehmkuhler, F.; Schulz, F.; Lokteva, I.; Parak, W.J.; Lehmkuhler, F. Recent Notable Approaches to Study Self-Assembly of Nanoparticles with X-Ray Scattering and Electron Microscopy. *Part. Part. Syst. Charact.* **2021**, *38*, 2100087. [CrossRef]
31. Li, R.; Bian, K.; Wang, Y.; Xu, H.; Hollingsworth, J.A.; Hanrath, T.; Fang, J.; Wang, Z. An Obtuse Rhombohedral Superlattice Assembled by Pt Nanocubes. *Nano Lett.* **2015**, *15*, 6254–6260. [CrossRef]

Disclaimer/Publisher’s Note: The statements, opinions and data contained in all publications are solely those of the individual author(s) and contributor(s) and not of MDPI and/or the editor(s). MDPI and/or the editor(s) disclaim responsibility for any injury to people or property resulting from any ideas, methods, instructions or products referred to in the content.